Magmatic degassing as the primary source of salt in Archean oceans

Eemu Ranta[1*], Tobias Fusswinkel[2], Christoph Beier[1], Enikő Bali[3]

[1]Department of Geosciences and Geography, University of Helsinki, Gustaf Hällströmin katu 2, 00560 Helsinki, Finland

[2]Institute of Applied Mineralogy and Economic Geology, RWTH Aachen University, Wüllnerstraße 2, 52062 Aachen, Germany

[3]Institute of Earth Sciences, University of Iceland, Sturlugata 7, 102 Reykjavík, Iceland

**corresponding author*

Supplemental material

Content

S1 METHODS

S1.1 Petrography

Rock samples used in the study (5A-series; 64.25560N, –14.98963E) were collected from the Vesturhorn volcanic complex in East Iceland (Roobol, 1974; Mattson et al., 1986; Law et al., 2024). Fluid inclusion and host quartz compositions were determined by laser ablation inductively coupled plasma mass spectrometry (LA-ICP-MS) at RWTH Aachen (Table S1). Sample mineralogy, textural relationships and fluid inclusion phase transformations were investigated using optical and CL microscopy, conventional microthermometry and back-scattered electron (BSE) imaging at HelLabs, University of Helsinki, and with Raman spectroscopy at RWTH Aachen. Feldspar compositions were measured at HelLabs by electron microprobe microanalysis (EPMA; Table S2). The investigated miarolitic cavities host two generations of quartz labeled Phase 1 and Phase 2 (Fig. S1A–D). The green hand sample colour of the Phase 2 overgrowths is caused by abundant fibrous to acicular actinolite inclusions which are absent in Phase 1 quartz. In addition to quartz, the cavities host large (> 0.5 cm) euhedral calcite crystals (with or without actinolite inclusions), actinolite needles growing in free space, and Fe-Ti-oxide (Fig. S1B). The mineralised cavities are surrounded by an alteration halo consisting of K-feldspar (Or_{95}) + albite ($Ab_{90–95}$) + Ba-feldspar (up to 18.6 mol.% Ba-feldspar end-member) + quartz (Phase 1) + calcite + Fe-Ti-oxide ± zircon ± apatite (Fig. S1C). The low-An feldspars completely or partly replace primary gabbroic plagioclase, which in the aplitic part has an

andesine composition ($An_{30–42}$). The investigated brine inclusions all occur in the high-T Phase 1 quartz (Fig. 1A). Other observed liquid- or vapor-rich fluid inclusion assemblages are either ambiguous with respect to textural context or are associated with the low-T Phase 2 quartz, and were not considered further in the present work. The Phase 1 quartz brine inclusions are always observed in assemblages together with vapor-rich inclusions (Fig. S1D-E). The vapor inclusions appear to be H_2O-dominated and low-salinity fluids, with the vapor phase showing distinct CO_2 Raman peaks at 1248 and 1388 cm^{-1} and, on a few occasions, a H_2S peak at 2612 cm^{-1} (Fig. S6). The LA-ICP-MS measurements of the vapor inclusions yield only low Cl peaks, with most trace elements including Br-I being below limits of detection. Visually, the vapor inclusions appear to trap variable amounts of brine, making inferences of the pure vapor phase trace element contents challenging and precluding determination of the halogen composition of the pure vapor phase.

S1.2 Electron probe microanalysis

Compositions of felspars in the alteration halo around the miarolitic cavity were determined by EPMA using a JEOL JXA-iSP100 Superprobe, equipped with 5 wavelength-dispersive spectrometers, at HelLabs at the University of Helsinki. An accelerating voltage of 15 kV and beam current of 15 nA, and a defocused beam with a 5 μm diameter was used with peak/background measurement times of 20/10s for all elements except Fe, Ti, Sr and Ba (40/20s). The element/detector/standard setup was: Na/TAPL/Astimex-albite, Mg/TAPL/Astimex-diopside, Fe/LIFL/Astimex-Cr-diopside, Ti/LIFL/Asimex-benitoite, K/PETH/Astimex-sanidine, Ca/PETH/Astimex-diopside, Sr/PETH/Asimex-celestite, Ba/PETH/Astimex-barite, Si/TAPL/Asimex-olivine, Al/TAPL/Astimex-albite. Matrix corrections were performed using the built-in ΦPZ Armstrong method. Accuracy (difference from reference value) and precision (2 relative standard deviations of the mean) were both better than 2% for Si, Na, Al and K, monitored with repeat measurements of the Astimex $An_{58.8}$ reference plagioclase.

S1.3 Fluid inclusion compositional analysis

Trace elements in the FIs and their host quartz were determined by LA-ICP-MS, performed using a GeoLAS HD 193 nm excimer laser ablation system coupled to an Agilent 7900s ICP-MS instrument at RWTH Aachen. The FI analytical setup follows the method optimized for triple halogen (Cl-Br-I) analysis in single fluid inclusions, outlined in Fusswinkel et al. (2018, 2022). A custom-made small-volume ablation cell with fast wash-out was used for the FI analyses. Teflon tubing and high-purity He carrier gas, filtered with a gas getter, were used to minimize the Cl, Br and I blanks. The analyzed isotopes were ^{7}Li, ^{11}B, ^{23}Na, $^{24,25}Mg$, ^{27}Al, ^{29}Si, ^{31}P, ^{34}S, ^{35}Cl, ^{39}K, ^{44}Ca, $^{47,49}Ti$, ^{55}Mn, $^{56,57}Fe$, ^{59}Co, ^{60}Ni, ^{65}Cu, ^{66}Zn, ^{75}As, ^{81}Br, ^{85}Rb, ^{88}Sr, ^{95}Mo, ^{107}Ag, ^{118}Sn, ^{121}Sb, ^{127}I, ^{133}Cs, ^{137}Ba, ^{182}W, ^{197}Au, ^{205}Tl, ^{208}Pb. Dwell times were 6 ms for ^{35}Cl, ^{81}Br and ^{127}I and 2 ms for the remaining masses. Figure S5 shows a typical LA-ICP-MS raw signal for a 15 μm diameter brine inclusion analysis. Fluid inclusions were

ablated with a laser fluency of 10 J/cm^2 and a pulse frequency of 10 Hz. Tuning was performed daily to optimize signal-to-noise ratio and to ensure low oxide production (ThO/Th < 0.2%), low mass fractionation (U/Th = 1.00±0.02) and low doubly charged ion production (Ca^{2+}/Ca^{+} < 0.4%). Instrumental accuracy was monitored by measurements of NIST613 reference glass as a secondary standard. The Sca17 scapolite (Fusswinkel et al., 2018) was used as an external calibration standard for Cl, Br and I, and the NIST611 reference glass for all other elements (Jochum et al., 2011). Both standards were measured at the beginning and end of each analytical session, as well as mid-session in approximately 3h intervals, to correct for instrumental sensitivity drift. The LA-ICP-MS signals were reduced using the PySILLS software (v1.0.62; Beeskow, 2024). ^{29}Si was used as an internal standard for quantifying quartz measurements, and for removing the background host quartz signal from the FI signals. ^{23}Na was used as an internal standard for reducing the FI data. Because of the multi-cation composition of the brines (Na-K-Fe-chloride), conventional microthermometry methods could not be reliably used to deduce FI Na concentrations. Hence we report all data normalised to Na. Since different data reduction schemes used in FI studies can yield different absolute element concentrations (Liu et al., 2024), it is worth noting that all plots and interpretations in this work are based on elemental ratios rather than absolute concentrations, which are unaffected by the choice of data reduction method. Only element abundances exceeding the limit of quantification (LOQ ≈ 3 times limit of detection (Beeskow, 2024) are reported in Table S1. Gold contents yielded values below LOQ for all analysed fluids. For vapor inclusions, the Br and I concentrations are below LOQ for all except two analysed FIs. For the brine inclusions, the propagated analytical uncertainty for the Br/Cl and I/Cl ratios is on average 4 % and 11 % (2RSD), respectively.

S1.4 Raman spectroscopy

Raman spectroscopy was used for identification of fluid inclusion daughter phases and vapor species (CO_2 and H_2S, H_2O; Dubessy et al., 1989). Raman spectra were collected at RWTH Aachen with a Renishaw inVia instrument equipped with a Coherent Sapphire steady-state laser. Laser powers between 5 and 100 % were used with 5–20 s collection times and 2-3 acquisitions. Higher power was used for vapor and liquid phases, and lower power for solid phases that were observed to be susceptible to beam damage.

S1.5 Cathodoluminescence microscopy

The textural relationships of the FIs and host rocks were examined petrographically in 100–300 micrometer thick double polished sections by transmitted light and cathodoluminescence light (CL) microscopy. Lumic HC6-LM hot cathode CL microscope at HelLabs was used with an accelerating voltage of 10-14 kV and current of 0.04 to 0.10 mA. Images taken with a 5x lens with an Olympus DP73 camera. Exposure times were 8s for non-luminescent quartz, and from 0.8 to 2 s for other

phases, all with 1-5 averaged exposures (usually 1). Multiple frames were stitched digitally to form the mosaics in Fig. S1C–D.

S1.6 Microthermometry

Phase transformation temperatures of fluid inclusions were observed using a Linkam THMS600G freezing and heating stages (with a temperature range of –195 to +600 °C) under a petrographic microscope at the University of Helsinki and RWTH Aachen. Heating experiments were performed following LA-ICP-MS measurements and/or on separate chips to avoid risk of heating-induced modification of FI compositions. The last observed phase transformation below 600 °C in the brine inclusions is halite dissolution at 360–440 °C, with a vapor phase still remaining at 600 °C (the limit of the stage), supporting > 600 °C formation temperatures (Fig. S7). Quantitative $NaCl_{eq}$ determinations in the Na-K-Fe-Cl-H_2O system cannot be made using the halite dissolution temperature due lack of available thermodynamic data. However, using Eq. 2 of Bodnar and Vityk (1994), halite dissolution temperature range of 360–440 °C translates to $NaCl_{eq}$ of 43–52 wt.%. The equation is based on a simple H_2O–NaCl system and the obtained salinity should only be considered cursory.

S1.7 Quantification of magmatic brine production in the Archean

To estimate the rate at which magmatic brines could transfer Cl to the Archean oceans, we here assume a similar brine production rate in the Archean to modern day Iceland (90–226 × 10^6 kg/yr of 16 wt% $NaCl_{eq}$ brine, equivalent to a brine chlorine flux (B_{Cl}) of 9–23 × 10^6 kg Cl/yr; Ranta et al., 2021). Assuming that all brine in Iceland is sourced from primary magma production, we estimate a brine production fraction F_{Cl} by

$$F_{Cl} = B_{Cl} / m_{Iceland} \quad \text{Eq. S1}$$

where $m_{Iceland}$ is the primary magma production rate in kg/yr. $m_{Iceland}$ was calculated as

$$m_{Iceland} = (V_E \times X + V_E) \times \rho_{melt} \quad \text{Eq. S2}$$

where V_E is the volumetric Icelandic eruption rate (we use 0.04–0.06 km^3/yr estimated for the Holocene (Thordarson and Larsen, 2007), X is the intrusive/extrusive (a value of 5 was used, deemed feasible for Iceland (White et al., 2006) and ρ_{melt} is the magma density (2750 kg/m^3 was used). These values yield $m_{Iceland}$ = 7–10 × 10^{11} kg/yr, which is similar to previous estimates (Ranta et al., 2023), and F_{Cl} = 19-6+3 × 10^{-5} kg Cl/kg magma. Notably, the F_{Cl} value of ~20 ppm represents 20 % of a typical Cl content of an Icelandic basalt of 100 ppm (Halldórsson et al., 2016), which matches with

equilibrium fluid exsolution amounts estimated for Vesturhorn based on Br/Cl and I/Cl ratios (Fig. S8). Model curves in Fig. S9 are calculated by the equation

$$Cl_{tot} = m_{Archean} \times F_{Cl} \times t \quad \text{Eq. S3}$$

where Cl_{tot} is the amount of Cl (in kg) in magmatic brines produced over time t (in yr), and $m_{Archean}$ is the Archean oceanic magma production rate in kg/yr. The latter can be estimated as

$$m_{Archean} = X_{spreading} \times A_{modern} \times D_{crust} \times \rho_{melt} \quad \text{Eq. S4}$$

where A_{modern} is the areal modern oceanic crust production rate (3 km^2/yr; Kendrick et al., 2020) , D_{crust} is the Archean oceanic crustal thickness in km (25–35 km; Herzberg et al., 2010) and $X_{spreading}$ is the ratio between the Archean and modern mid-ocean spreading rates (2–3; Bickle, 1986). It is feasible to assume that these calculation represents a conservative estimate of Archean magmatic brine production rate for two reasons: First, the Cl concentrations of the primary mantle may have been 5 times higher relative to the modern mantle because the modern crustal reservoirs and hydrosphere hold >80% of Earth's chlorine (Kendrick et al., 2017). This would imply higher F_{Cl} and higher brine production rates in the Hadean and early Archean. Second, the equation for Cl_{tot} only considers oceanic crust produced at mid-ocean ridges. A significant, but poorly constrained proportion of the Archean crust was likely formed as thickened oceanic plateaus by plume magmatism (formed at a mass rate $m_{plateau}$), and in emerging proto-continents (formed at a mass rate $m_{continent}$), which were both mostly submerged by oceans (Cawood and Hawkesworth, 2019). A Cl production equation that accounts for these additional magma sources would have two added mass rate terms:

$$Cl_{tot} = (m_{Archean} + m_{plateau} + m_{continent}) \times F_{Cl} \times t \quad \text{Eq. S5}$$

Together, these considerations suggest that magmatic brines production may have been higher, and could have salinated the oceans earlier than implied by Fig. S9.

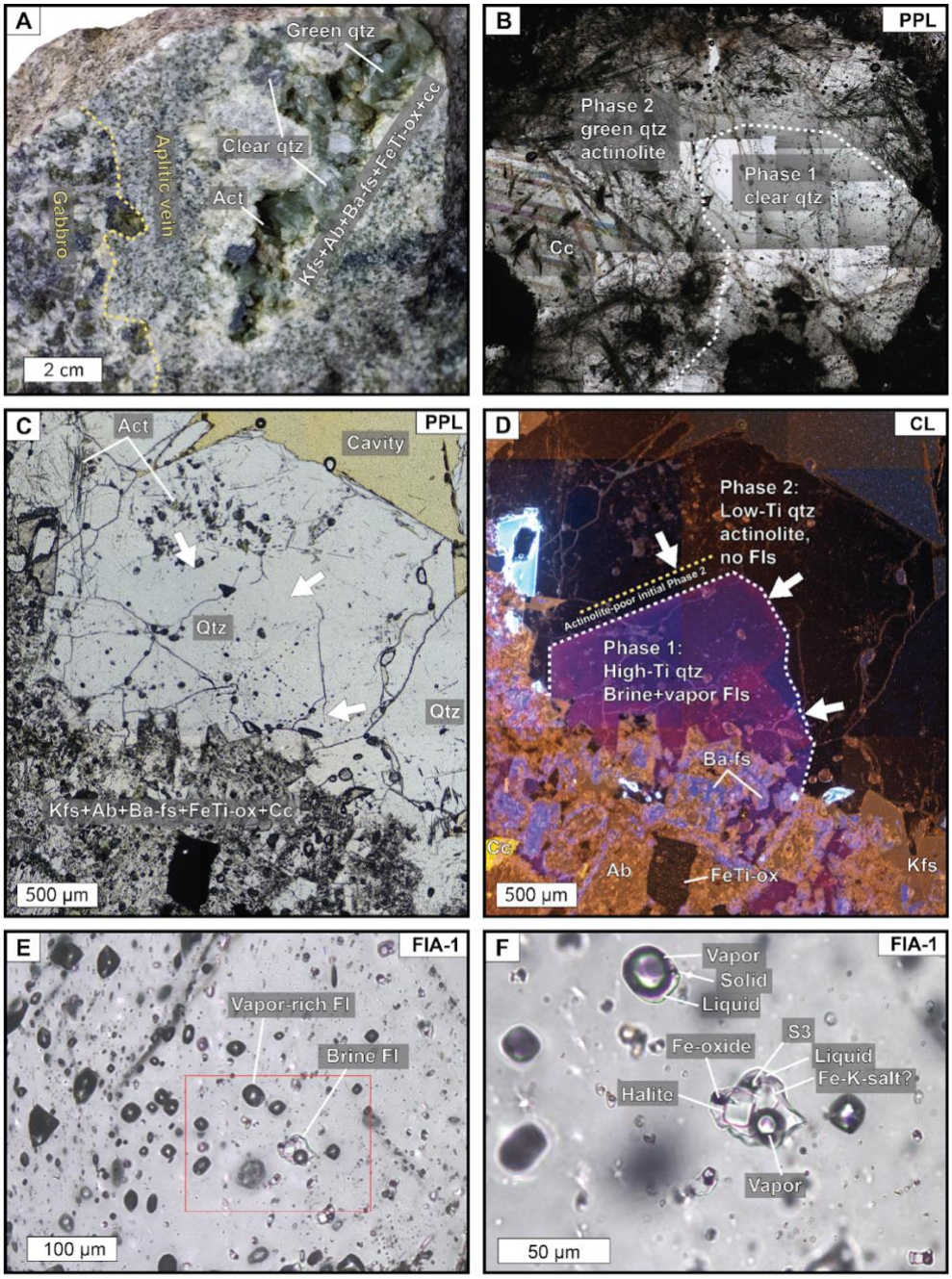

Figure S1. Petrography. (A) Sample 5A with free-growing quartz and actinolite in an exposed miarolitic cavity. The cavity is surrounded by an alteration rim, an aplitic zone and the host gabbro. (B) Thick section image mosaic of green and clear quartz and calcite growing within a cavity. Fluid inclusions are limited to actinolite-free Phase 1 quartz. (C) Thin section image of euhedral quartz in the miarolitic cavity, with an actinolite-bearing growth rim and an actinolite-free core (D) Cathodoluminescence (CL) image of the same view as in (C). The fluid inclusion-bearing phase 1 quartz is free of actinolite inclusions and has purple-to-violet CL colors suggesting a high-T origin (Müller et al. 2000, Richter and Diamond 2022). Zircon shows light blue CL colors. (E) A depth-stacked image of a typical fluid inclusion assemblage in Phase 1 quartz with co-existing vapor-rich and brine fluid inclusions. The area within the red rectangle is blown up in (F): Close up of the two inclusion types. The brine inclusions host a variable amount of vapor, liquid and typically 3–4 solid phases at 20°C: a translucent green rectangular solid (S1, halite), a second transparent anhedral solid (S2), a yellow transparent solid (S3; not present in all assemblages), and an opaque phase (S4). Based on Raman spectra and detailed inspection of LA-ICP-MS signals, the solid phases are two different (S1 and S2), Mg-sulfate (S3) and a Fe-oxide (S4). The vapor-rich inclusions often host an oxide and/or a Na-K-Fe chloride.

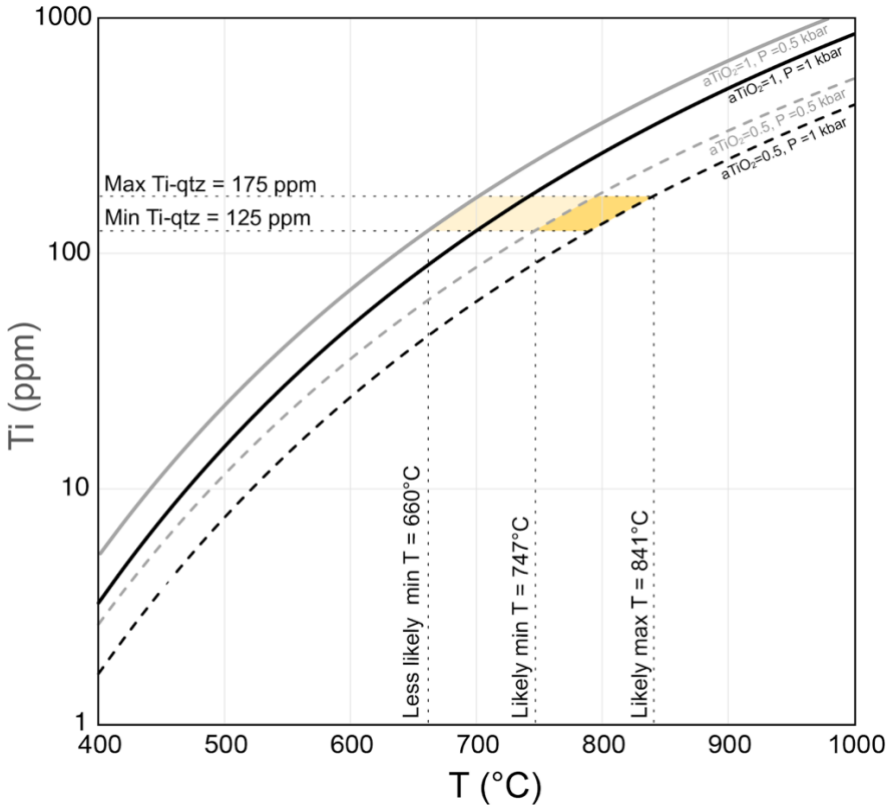

Figure S2. Ti-in-quartz thermometry. The Ti-in-qtz thermometer (Huang and Audétat 2012) indicates quartz formation temperatures of 750–840 °C, using the observed range of 150±25 ppm Ti, and assuming formation conditions between 0.5–1 kbar and a Ti activity of $aTiO_2$ = 0.5. This $aTiO_2$ was chosen due to the presence of Fe-Ti-oxides, and lack of observed rutile, in the miarolitic cavities. Higher Ti activities would yield lower temperatures of down to 660 °C at $aTiO_2$ = 1.0 and 125 ppm Ti, which is considered to be the minimum formation temperature of the Phase 1 quartz.

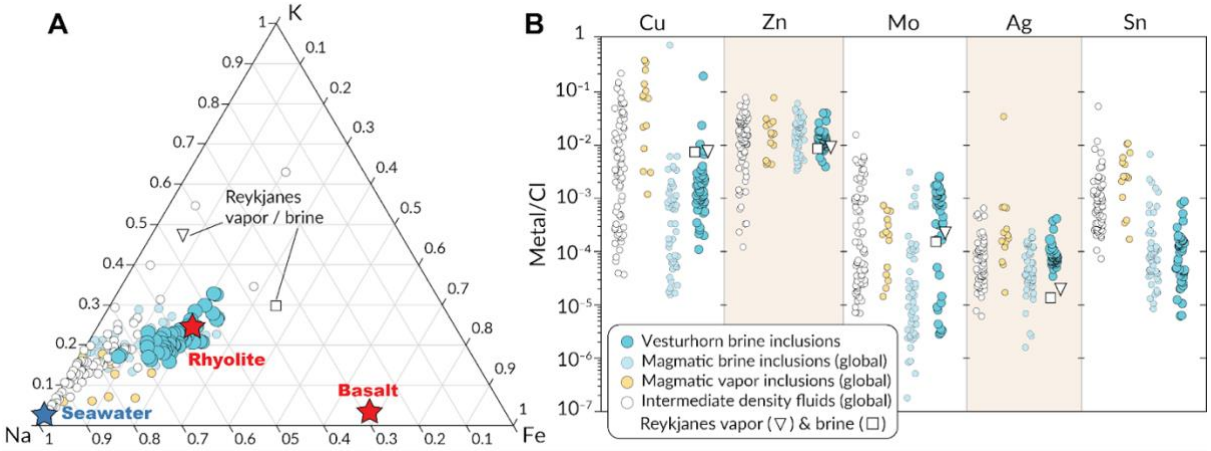

Figure S3. Major cation and trace metal compositions of brine inclusions. (A) Na-K-Fe molar compositions. The Vesturhorn brines have high K and Fe relative to Na, overlapping with average Icelandic rhyolite compositions (average of published silicic MIs; IMIC database of Ranta et al. 2024). (B) The Cl-normalised brine Cu-Zn-Mo-Ag-Sn contents overlap with magmatic brine compositions from continental granitic settings (including both barren and porphyry ore-forming systems) as well as high-T (600 °C) vapor and brine inclusion compositions from an active hydrothermal system in the Reykjanes Peninsula, Iceland, from Bali et al. (2020). Comparative data for magmatic vapor, brine and intermediate density fluid from compilation of Hogg et al. (2023) that includes data from Audétat (2019), Audétat and Pettke (2003), Audétat and Zhang (2019), Audétat et al. (2008), Zajacz et al. (2008), Seo et al. (2009), William-Jones and Heinrich (2005).

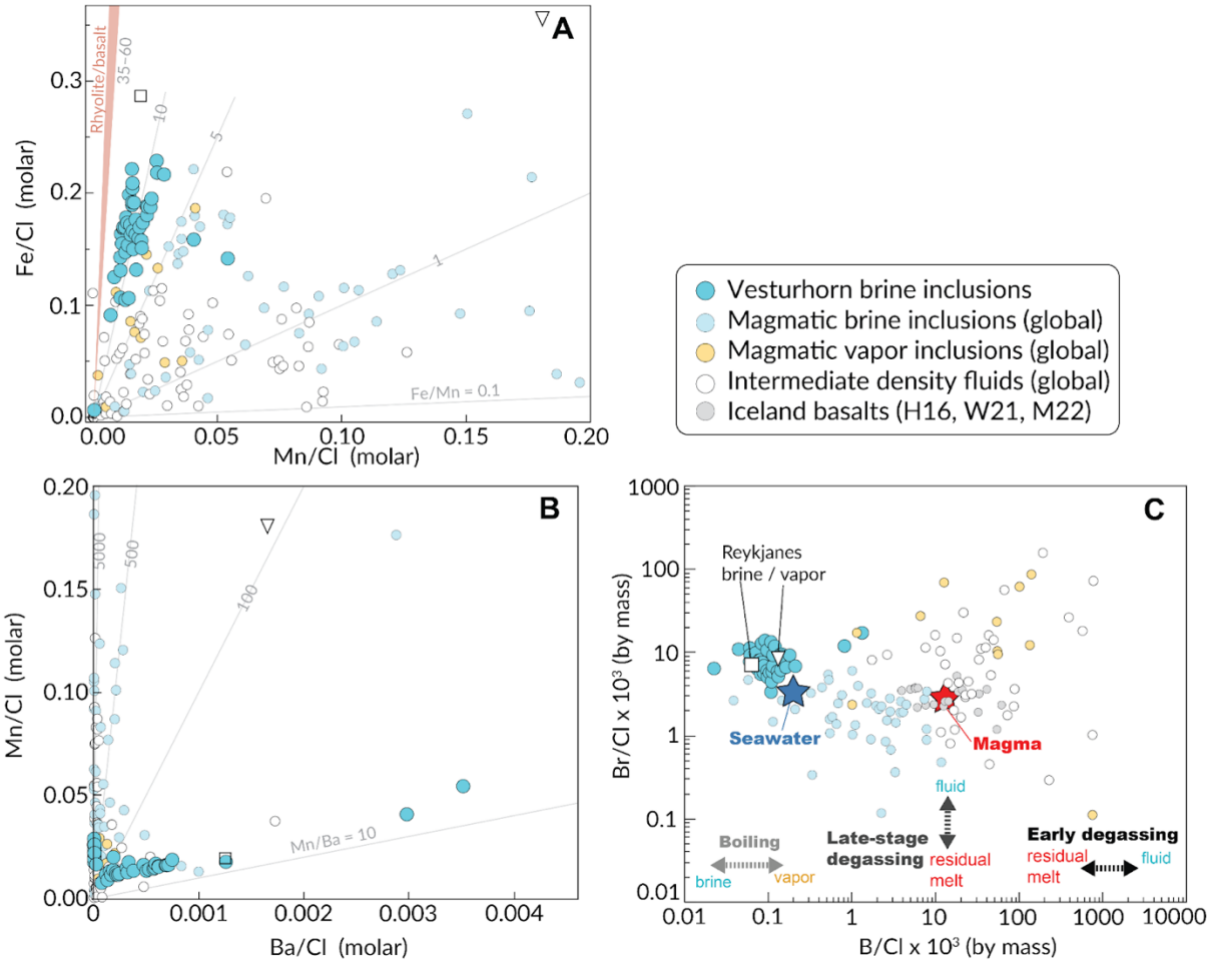

Figure S4. (A) and (B) show the Fe-Mn-Ba systematics systematics of the Vesturhorn brines. (C) The B/Cl and Br/Cl ratios have been used in the fluid inclusion literature to discern between magmatic and seawater sources. However, the B/Cl brine signature is fractionated by both early degassing (i.e., potentially prior to major NaCl-H_2O phase exsolution) and by boiling, due to preferential partitioning of B to the vapor phase in both cases (Schatz et al. 2004). The B/Cl fractionation during phase-separation is illustrated by high B/Cl of published magmatic vapor data relative to brines (see Fig. S3 for data references). The Br/Cl and I/Cl ratios, which do not fractionate during phase separation, are hence more suitable tracers of seawater vs. magmatic fluid sources. The parental melt compositions for the fluid inclusion literature data are not known. In general, the new Vesturhorn fluid inclusion data show strikingly similar major cation concentrations as well as Br/Cl and B/Cl ratios to high-T fluid inclusions from the IDDP-2 well drilled into the active Reykjanes geothermal system in Iceland (Bali et al. 2020). Iceland basalt data from Halldórsson et al. (2016), Waters (2021), Marshall et al. (2022).

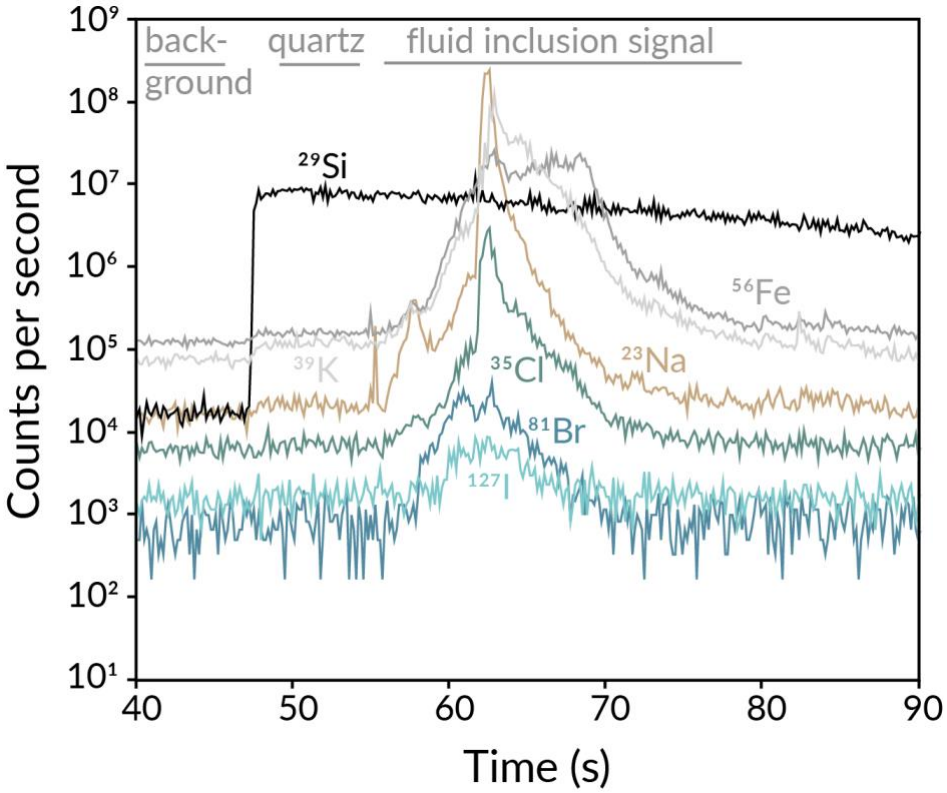

Figure S5. Example LA-ICP-MS signal of a quartz-hosted, 15 micron-diameter brine inclusion (24_04_10_b18). The inclusion was located about 20 µm below the surface and was ablated with a 32 µm diameter circular beam. Only a selection of the analysed elements is shown for clarity.

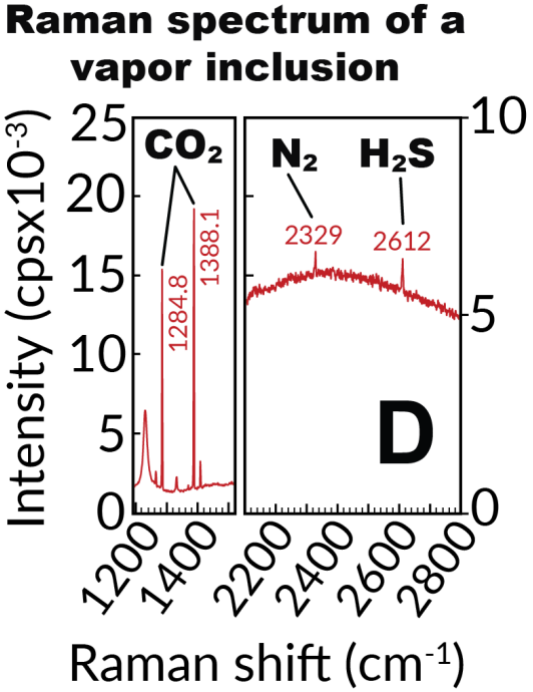

Figure S6. Raman spectrum of a vapor-rich inclusion, indicating presence of minor CO_2 and trace H_2S, compatible with a late-stage magmatic origin. The N_2 peak is room air.

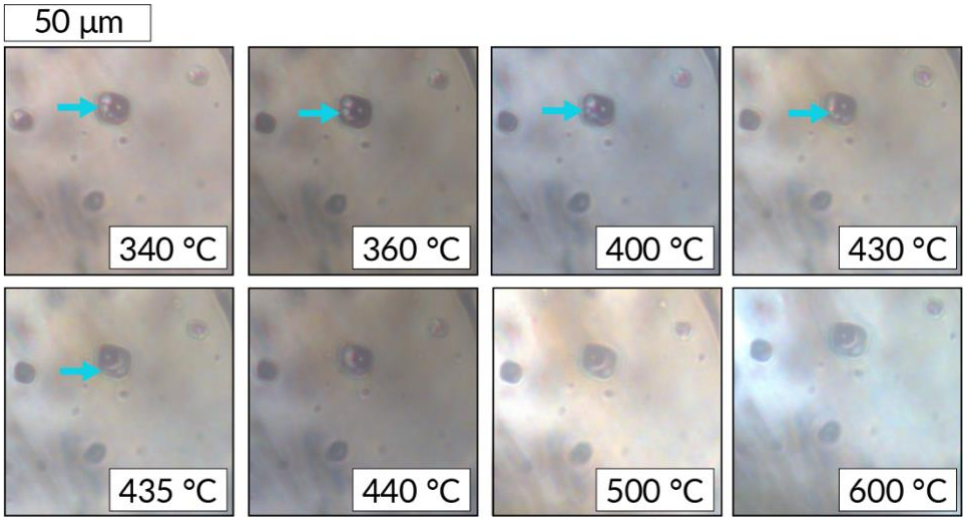

Figure S7. Heating experiment. The figure shows a representative Vesturhorn brine inclusion during heating to 600 °C. Halite (blue arrow) dissolves at ~436 °C. A vapor bubble is present in all visible inclusions still at 600 °C.

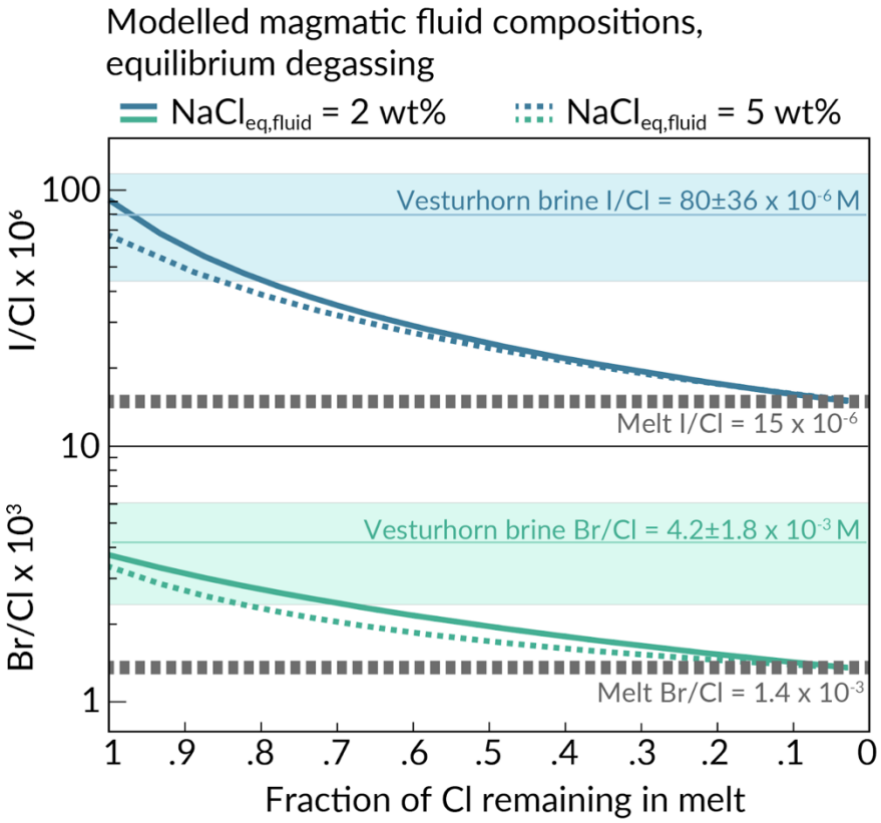

Figure S8. Equilibrium fluid exsolution model. The curves show the I/Cl and Br/Cl evolution of an equilibrium fluid exsolved from a melt with Br/Cl and I/Cl ratios of an average Icelandic basalt (Waters 2021). The modelled fluid compositions overlap with measured brine compositions at F > 0.8 (fraction of Cl remaining in the melt). This is consistent with a relatively modest observed loss of Cl observed between crystalline lavas and estimated melt compositions (e.g. Sigvaldason and Óskarsson 1976). It is assumed that fractional crystallization of the basaltic melt to rhyolitic compositions does not fractionate Br/Cl and I/Cl ratios. The models are calculated using a closed-system equilibrium mass balance equation. The fluid-melt partition coefficients for Cl, Br and I were calculated using Eqs. 2–4 of Miranda et al. (2025), with average silicic melt inclusion compositions from Iceland (from the IMIC database of Ranta et al. 2024) used to determine the compositional terms (Table S4). Fluid salinites of $NaCl_{eq}$ = 2 and 5 wt.% were assumed for a one-phase fluid exsolved from a silicic Icelandic melt (cf. Ranta et al. 2021), yielding partition coefficients of $D_{f\text{-}m}$(Cl) = 37–64, $D_{f\text{-}m}$(Br) = 102–158, $D_{f\text{-}m}$(I) = 227–285.

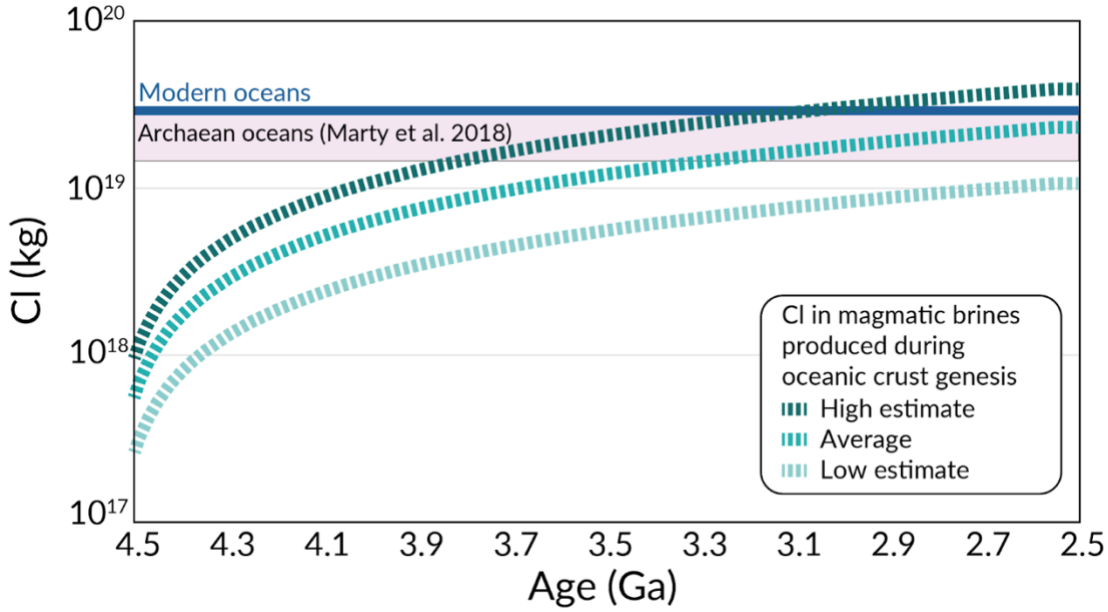

Figure S9. Estimated mass of Cl produced by magmatic fluid exsolution during generation of early oceanic crust. Mass of Cl in the modern and Archean oceans, estimated as 0.5–1 times modern (Marty et al. 2018), are plotted as a blue line and a pink box, respectively. Calculation parameters are given in Table S5.

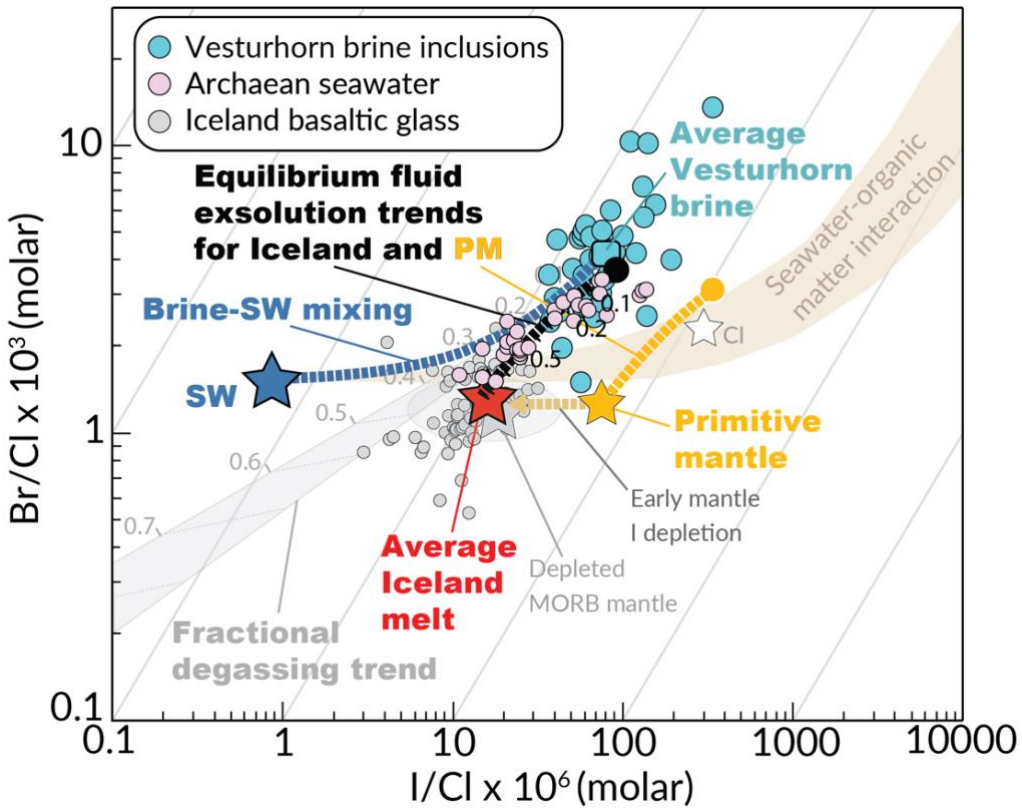

Figure S10. Halogen systematics. Fractional degassing (grey envelope; calculated after Aiuppa, 2009) of an average Iceland melt yields a similar degassing trend to the equilibrium model (calculated as in Fig.1) at F < 0.3. Tic marks indicate the fraction F of degassed chlorine. Brine-modern seawater (SW) mixing (blue dashed line) on Cl-Br-I on fluid halogen compositions demonstrates the lack of a seawater component in the Vesturhorn fluids. Iceland glass data are from Weston (2013) and Waters (2021), Archean seawater data from Channer et al. (2017) and Burgess et al. (2020)

References

Aiuppa, A., 2009, Degassing of halogens from basaltic volcanism: Insights from volcanic gas observations. Chemical Geology: v. 263(1-4), p. 99-109.

Audétat, A., 2019, The metal content of magmatic-hydrothermal fluids and its relationship to mineralization potential: Economic Geology, v. 114(6), p. 1033-1056.

Audétat, A., and Pettke, T., 2003, The magmatic-hydrothermal evolution of two barren granites: A melt and fluid inclusion study of the Rito del Medio and Canada Pinabete plutons in northern New Mexico (USA): Geochimica et Cosmochimica Acta, v. 67(1), p. 97-121.

Audétat, A., and Zhang, D., 2019, Abundances of S, Ga, Ge, Cd, In, Tl and 32 other major to trace elements in high-temperature (350–700° C) magmatic-hydrothermal fluids: Ore Geology Reviews, v. 109, p. 630-642.

Audétat, A., Pettke, T., Heinrich, C.A., and Bodnar, R.J., 2008, Special paper: the composition of magmatic-hydrothermal fluids in barren and mineralized intrusions: Economic Geology, v. 103(5), p. 877-908.

Bali, E., Aradi, L. E., Zierenberg, R., Diamond, L. W., Pettke, T., Szabó, Á., ... and Szabó, C., 2020, Geothermal energy and ore-forming potential of 600 °C mid-ocean-ridge hydrothermal fluids: Geology, v. 48(12), p. 1221-1225.

Beeskow M.A., 2024, PySILLS: LA-ICP-MS analysis (v.1.0.62) https://github.com/MABeeskow/PySILLS.

Bickle, M.J., 1986, Implications of melting for stabilisation of the lithosphere and heat loss in the Archaean: Earth and Planetary Science Letters, v. 80(3-4), p. 314-324.

Bodnar, R.J., and M.O. Vityk, 1994, Interpretation of microthermometric data for H_2O-NaCl fluid inclusions, in De Vivo, B., and Frezzotti, M.L., eds., Fluid Inclusions in Minerals, Methods and Applications, Virginia Tech, Blacksburg, VA, p. 117-130.

Burgess, R., Goldsmith, S.L., Sumino, H., Gilmour, J.D., Marty, B., Pujol, M., and Konhauser, K.O., 2020, Archean to Paleoproterozoic seawater halogen ratios recorded by fluid inclusions in chert and hydrothermal quartz: American Mineralogist, v. 105(9), p. 1317-1325.

Channer, D.D., de Ronde, C.E.J., and Spooner, E.T.C., 1997, The Cl-Br-I-composition of~ 3.23 Ga modified seawater: implications for the geological evolution of ocean halide chemistry: Earth and Planetary Science Letters, v. 150(3-4), p. 325-335.

Dubessy, J., Poty, B., and Ramboz, C., 1989, Advances in COHNS fluid geochemistry based on micro-Raman spectrometric analysis of fluid inclusions: European journal of Mineralogy, v. 1(4), p. 517-534.

Fusswinkel, T., Giehl, C., Beermann, O., Fredriksson, J.R., Garbe-Schönberg, D., Scholten, L., and Wagner, T., 2018, Combined LA-ICP-MS microanalysis of iodine, bromine and chlorine in fluid inclusions: Journal of Analytical Atomic Spectrometry, v. 33(5), p. 768-783.

Fusswinkel, T., Niinikoski-Fusswinkel, P., and Wagner, T., 2022, Halogen ratios in crustal fluids through time—Proxies for the emergence of aerobic life?: Geology, v. 50(10), p. 1096-1100.

Halldórsson, S. A., Barnes, J.D., Stefánsson, A., Hilton, D.R., Hauri, E.H., and Marshall, E.W., 2016, Subducted lithosphere controls halogen enrichments in the Iceland mantle plume source: Geology, v. 44(8), p. 679-682.

Herzberg, C., Condie, K., and Korenaga, J., 2010, Thermal history of the Earth and its petrological expression: Earth and Planetary Science Letters, v. 292(1-2), p. 79-88.

Hogg, O.R., Edmonds, M., and Blundy, J., 2023, Water-rich magmas optimise volcanic chalcophile element outgassing fluxes: Earth and Planetary Science Letters, v. 611, 118153.

Jochum, K.P., Weis, U., Stoll, B., Kuzmin, D., Yang, Q., Raczek, I., ... and Enzweiler, J., 2011, Determination of reference values for NIST SRM 610–617 glasses following ISO guidelines: Geostandards and Geoanalytical Research, v. 35, p. 397–429.

Kendrick, M.A., Hémond, C., Kamenetsky, V.S., Danyushevsky, L., Devey, C.W., Rodemann, T., ... and Perfit, M.R., 2017, Seawater cycled throughout Earth's mantle in partially serpentinized lithosphere: Nature Geoscience, v. 10(3), p. 222-228.

Kendrick, M.A., Danyushevsky, L.V., Falloon, T.J., Woodhead, J.D., Arculus, R.J., and Ireland, T., 2020, SW Pacific arc and backarc lavas and the role of slab-bend serpentinites in the global halogen cycle: Earth and Planetary Science Letters, v. 530, 115921.

Law, S., Hastie, A.R., Young, L.A., and Thordarson, T., 2024, Formation of silicic crust on early Earth and young planetary bodies in an Iceland-like setting: Communications Earth and Environment, v. 5(1), 350.

Liu, Y., Wagner, T., and Fußwinkel, T., 2024, An integrated approach for quantifying fluid inclusion data combining microthermometry, LA-ICP-MS, and thermodynamic modeling: Chemical Geology, v. 644, 121863.

Lodders, K., and Fegley Jr, B., 2023,. Solar system abundances and condensation temperatures of the halogens fluorine, chlorine, bromine, and iodine: Geochemistry, v. 83(1), 125957.

Marshall, E.W., Ranta, E., Halldórsson, S.A., Caracciolo, A., Bali, E., Jeon, H., ... and Stefánsson, A., 2022, Boron isotope evidence for devolatilized and rehydrated recycled materials in the Icelandic mantle source: Earth and Planetary Science Letters, v. 577, 117229.

Mattson, S.R., Vogel, T.A., and Wilband, J.T., 1986, Petrochemistry of the silicic-mafic complexes at Vesturhorn and Austurhorn, Iceland: evidence for zoned/stratified magma: Journal of Volcanology and Geothermal Research, v. 28(3-4), p. 197-223.

Müller, A., Seltmann, R., and Behr, H.J. (2000). Application of cathodoluminescence to magmatic quartz in a tin granite–case study from the Schellerhau Granite Complex, Eastern Erzgebirge, Germany: Mineralium Deposita, v. 35, p. 169-189.

Ranta, E., Halldórsson, S.A., Barnes, J.D., Jónasson, K., and Stefánsson, A., 2021, Chlorine isotope ratios record magmatic brine assimilation during rhyolite genesis: Geochemical Perspectives Letters, v. 16, p. 35–39.

Ranta, E., Halldórsson, S.A., Barry, P.H., Ono, S., Robin, J.G., Kleine, B.I., ... and Stefánsson, A., 2023, Deep magma degassing and volatile fluxes through volcanic hydrothermal systems: Insights from the Askja and Kverkfjöll volcanoes, Iceland: Journal of Volcanology and Geothermal Research, v. 436, 107776.

Ranta, E., Halldórsson, S.A., Óladóttir, B.A., Pfeffer, M.A., Caracciolo, A., Bali, E., ... and Barsotti, S., 2024, Magmatic controls on volcanic sulfur emissions at the Iceland hotspot: Geochemistry, Geophysics, Geosystems, v. 25(5), e2024GC011443.

Richter, L., and Diamond, L.W., 2022, Characterization of hydrothermal fluids that alter the upper oceanic crust to spilite and epidosite: Fluid inclusion evidence from the Semail (Oman) and Troodos (Cyprus) ophiolites. Geochimica et Cosmochimica Acta, v. 319, p. 220-253.

Roobol, M.J., 1974, The geology of the Vesturhorn intrusion, SE Iceland: Geological Magazine, v. 111(4), p. 273-286.

Schatz, O.J., Dolejš, D., Stix, J., Williams-Jones, A.E., and Layne, G.D., 2004, Partitioning of boron among melt, brine and vapor in the system haplogranite–H_2O–NaCl at 800 C and 100 MPa: Chemical Geology, v. 210(1-4), p. 135-147.

Seo, J.H., Guillong, M., and Heinrich, C.A., 2009, The role of sulfur in the formation of magmatic–hydrothermal copper–gold deposits: Earth and Planetary Science Letters, v. 282(1-4), p. 323-328.

Sigvaldason, G.E., and Óskarsson, N., 1976, Chlorine in basalts from Iceland: Geochimica et Cosmochimica Acta, v. 40(7), p. 777-789.

Thordarson, T., and Larsen, G., 2007, Volcanism in Iceland in historical time: Volcano types, eruption styles and eruptive history: Journal of Geodynamics, v. 43(1), p. 118-152.

Weston, B.M., 2013, Noble gases and halogens in Icelandic basalts, Doctoral dissertation, The University of Manchester (United Kingdom), pp. 225.

Williams-Jones, A.E., and Heinrich, C.A., 2005, 100th Anniversary special paper: vapor transport of metals and the formation of magmatic-hydrothermal ore deposits: Economic Geology, v. 100(7), p. 1287-1312.

Zajacz, Z., Halter, W.E., Pettke, T., and Guillong, M., 2008, Determination of fluid/melt partition coefficients by LA-ICPMS analysis of co-existing fluid and silicate melt inclusions: Controls on element partitioning: Geochimica et Cosmochimica Acta, v. 72(8), p. 2169-2197.